Electronic Supplementary Information (ESI)

Construction of homologous bimetallic oxide $Bi_2Fe_4O_9$@$Bi_{25}FeO_{40}$ heterostructure to boost supercapacitor performance

Bingjie Cheng,[a] Xiaoqiang Li,[b] Ruqu Han,*[a] Jun Xiang,*[a] and Yamei Zhang[a]

[a] School of Science, Jiangsu University of Science and Technology, Zhenjiang 212100, PR China.

[b] Institute of Materials Science and Engineering, Beijing University of Technology, Beijing 100124, PR China.

*Corresponding authors.

E-mail addresses: rqhan@just.edu.cn (R. Han), jxiang@just.edu.cn (J.Xiang).

Experimental section

Materials

Nitric acid (HNO_3, 65%), bismuth nitrate pentahydrate ($Bi(NO_3)_3·5H_2O$, 99%), iron nitrate nonahydrate ($Fe(NO_3)_3·9H_2O$, 98.5%), ammonia ($NH_3·H_2O$, 25%), potassium hydroxide (KOH, 85%) and sodium hydroxide (NaOH, 96%) are purchased from Sinopharm Chemical Reagent Co., Ltd. and used as received. Polyvinylidene fluoride (PVDF), N-methylpyrrolidone (NMP), activated carbon (AC) and nickel foam (NF, surface density: 320 g m^{-2}) are obtained from Cyber Electrochemical Materials Web Store.

Sample preparation

Based on our previous work, the detailed experimental procedure was described here. Firstly, bismuth nitrate pentahydrate (2.45 g) and iron nitrate nonahydrate (4.10 g) were sequentially added to a solution consisting of 2.8 g of nitric acid and 13 g of deionized water mixed homogeneously and continuously stirred magnetically for 2 h to obtain a transparent solution with light yellow color. After that, 100 mL of deionized water and appropriate quantities of ammonia were slowly added to the above solution, and the residue gradually changed from yellow to brown, which was stirred magnetically sufficiently. Then the supernatant and the precipitate were separated completely by standing at room temperature for 24 h. Then the precipitate after centrifugation was redissolved into 60 mL of 12 M NaOH solution with uninterruptedly magnetic stirring for 24 h. The solution was transferred to a polytetrafluoroethylene liner, and the hydrothermal treatment was carried out in a programmable oven at 180 °C for 0.5, 1.0 and 2.0 h, respectively. The precipitates were centrifuged to remove impurity ions and dried thoroughly at 60 °C in a vacuum oven. The products obtained at the hydrothermal times of 0.5, 1.0 and 2.0 h were $Bi_{25}FeO_{40}$, $Bi_2Fe_4O_9$@$Bi_{25}FeO_{40}$ and $Bi_2Fe_4O_9$, respectively.

Preparation of electrodes

20 mg prepared sample, 2.5 mg acetylene black and 2.5 mg PVDF were sequentially weighed and placed in a mortar to grind thoroughly until the materials were homogeneously combined. Subsequently, the appropriate volume of NMP was added to form a slurry. Ultimately, the NF was uniformly coated by the slurry and treated in a vacuum oven at 55 °C for 24 h to form the electrodes. In this work, the effective mass over the collector is about 0.8 mg.

Assembly of $Bi_2Fe_4O_9$@$Bi_{25}FeO_{40}$//AC asymmetric supercapacitors (ASC)

The NF loaded with AC was used as the negative electrode, $Bi_2Fe_4O_9$@$Bi_{25}FeO_{40}$ as the positive electrode,

and 3 M KOH as the electrolyte to assemble $Bi_2Fe_4O_9$@$Bi_{25}FeO_{40}$//AC ASC according to the following Eq. S1.[1]

$$\frac{m_+}{m_-} = \frac{C_- V_-}{C_+ V_+} \quad \text{(S1)}$$

where, m_+, C_+ and V_+ are the effective active mass, specific capacitance and voltage window of $Bi_2Fe_4O_9$@$Bi_{25}FeO_{40}$, respectively; m_-, C_- and V_- stand for corresponding parameters of the AC.

Characterization

The morphology and microstructure of the samples were observed by scanning electron microscope (SEM, Zeiss Merlin Compact) and transmission electron microscope (TEM, JEOL JEM–2100). X-ray diffractometry (XRD, Rigaku SmartLab) was used to investigate the phase structure of materials. X-ray photoelectron spectroscopy (XPS, Thermo Scientific Nexsa) was used to characterize the elemental composition and chemical valence states and to analyze the surface matter of samples semi-quantitatively, in which the binding energies of all elements were calibrated with C 1s at 284.6 eV. UV-Vis diffuse reflectance spectra (DRS) were utilized to calculate the band gaps of the products by the Kubelka-Munk function based on the selective absorption at 400–1000 nm wavelength range. Mott-Schottky (MS) test was performed with a built-in saturated KCl solution of Ag/AgCl as the reference electrode, 0.5 M Na_2SO_4 as the electrolyte, and indium tin oxide (ITO) conductive glass coated with active material as the working electrode with 1000 Hz alternating current signal applied simultaneously. Nitrogen adsorption-desorption isotherms of the samples were recorded on a Micromeritics ASAP 2460 instrument at 77 K to quantify their specific surface area and pore structure using the Brunauer-Emmett-Teller (BET) method.

Electrochemical measurements

Hg/HgO was used as the reference electrode, Pt was as the counter electrode, and self-manufactured material was assembled with the collector as the working electrode. Subsequently, the three-electrode system was utilized to perform electrochemical performance tests on a Chenhua electrochemical workstation (CHI-660E). Electrochemical impedance spectra (EIS) were measured in the 0.01 Hz–100 KHz frequency range. Cyclic voltammetry (CV) tests were performed with a voltage window of 0.25–0.55 V. Additionally, based on the CV curves, the electrochemical kinetic behavior of the electrodes was evaluated by Eqs. S2-3.[2]

$$I_P = av^b \quad \text{(S2)}$$

$$\log I_P = b\log v + \log a \quad \text{(S3)}$$

where, I_p is the redox peaks' peak current (mA) in the CV curves, v is the scan rate (mV s^{-1}), and a and b represent

adjustable parameters. The slope of a line plotted with logI_p as the vertical coordinate and log$v$ as the horizontal coordinate is b. Significantly, b = 0.5 indicates that the electrochemical kinetic behavior is controlled by diffusion, while b = 1.0 demonstrates that the electrochemical kinetics is controlled by capacitance. Furthermore, the capacitance-control and the diffusion-control contribution percentage can be calculated by the Eq. S4.[3]

$$i(\mathrm{V}) = i_{\mathrm{cap}} + i_{\mathrm{diff}} = k_1 v + k_2 v^{1/2} \quad \text{(S4)}$$

where, $k_1 v$ is the capacitance-control component and $k_2 v^{1/2}$ is the diffusion-control component.

With the scan rate increasing from 5 mV s^{-1} to 100 mV s^{-1} in an orderly progression, it was used to determine the type of charge storage. The specific capacitance (C, F g^{-1}) was calculated by performing galvanostatic charge–discharge (GCD) tests under various current densities from 10.0 to 0.5 A g^{-1} according to Eq. S5.[4]

$$C = \frac{I \times \Delta t}{m \times \Delta V} \quad \text{(S5)}$$

where, I/m, Δt and ΔV are current density (A g^{-1}), discharge time (s) and voltage window (V), respectively.

A two-electrode system was used to characterize the electrochemical behavior of the $Bi_2Fe_4O_9$@$Bi_{25}FeO_{40}$//AC ASC device. The CV curves were used to identify the most appropriate operating voltage window and to measure the ASC device's current response at different scan rates. Energy density (E, Wh kg^{-1}) and power density (P, W kg^{-1}) of $Bi_2Fe_4O_9$@$Bi_{25}FeO_{40}$//AC ASC were calculated according to Eqs. S6-7.[5]

$$E = \frac{C \times \Delta V^2}{7.2} \quad \text{(S6)}$$

$$P = \frac{3600 \times E}{\Delta t} \quad \text{(S7)}$$

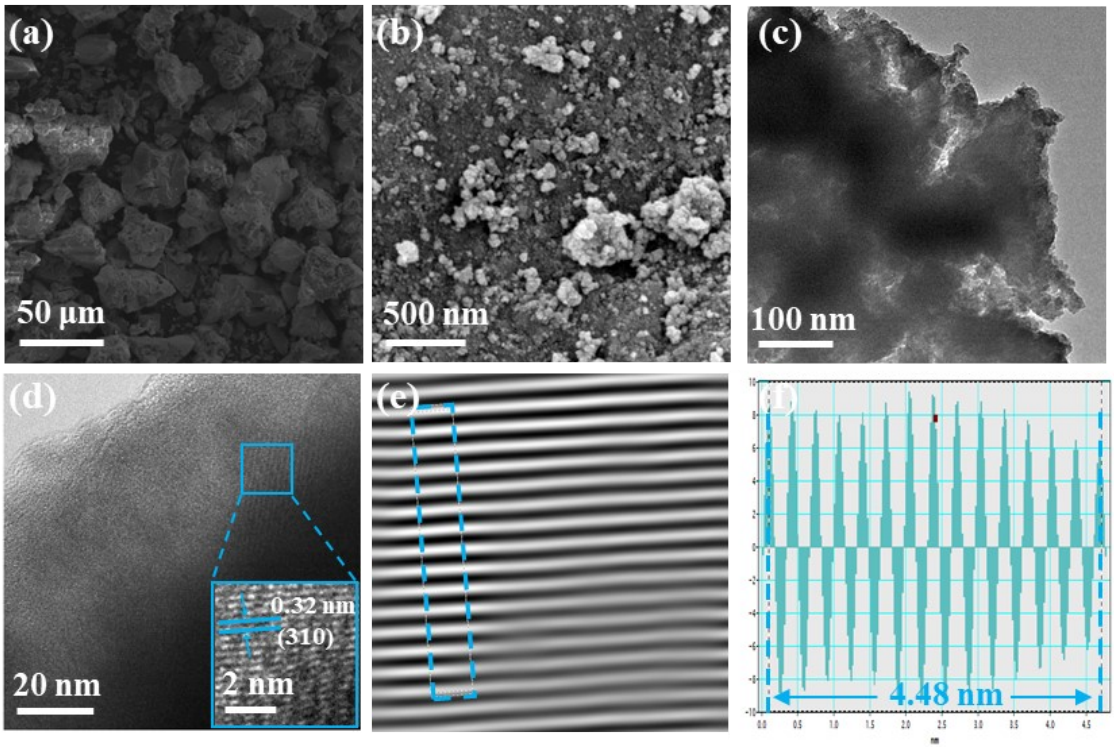

Fig. S1. (a-b) SEM, (c-d) TEM and (e-f) IFFT images of $Bi_{25}FeO_{40}$.

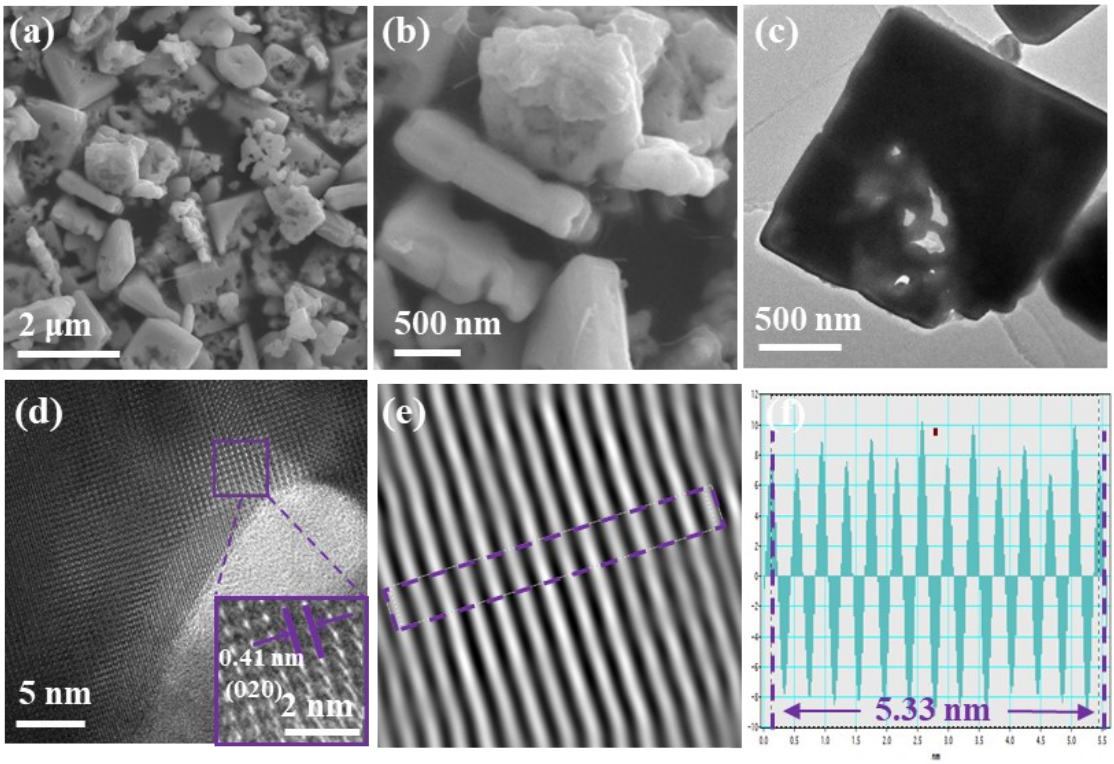

Fig. S2. (a-b) SEM, (c-d) TEM and (e-f) IFFT images of $Bi_2Fe_4O_9$.

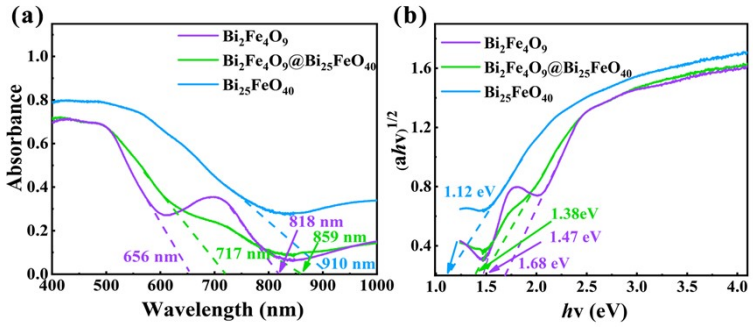

Fig. S3 (a) UV-vis diffuse reflectance spectra and (b) estimated band gaps of the samples.

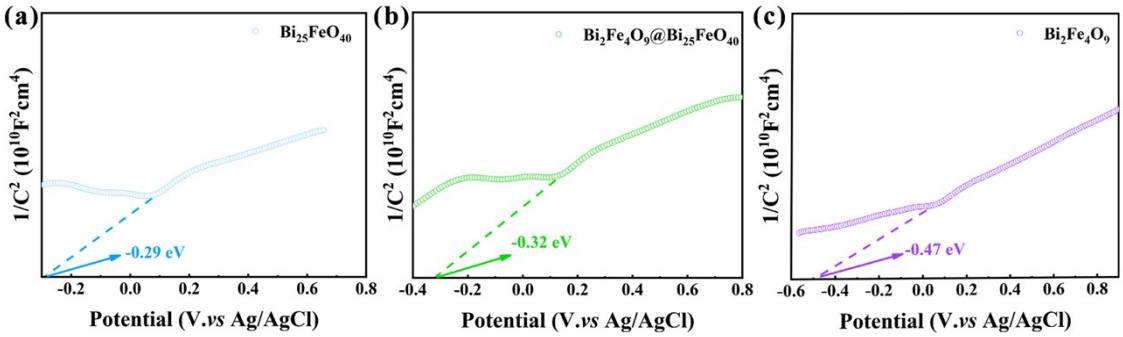

Fig. S4. Mott-Schottky plots of (a) $Bi_{25}FeO_{40}$, (b) $Bi_2Fe_4O_9$@$Bi_{25}FeO_{40}$ and (c) $Bi_2Fe_4O_9$.

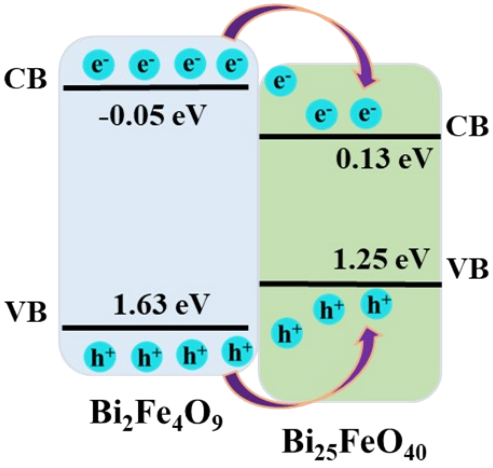

Scheme S1. Energy band structure of $Bi_2Fe_4O_9$ and $Bi_{25}FeO_{40}$

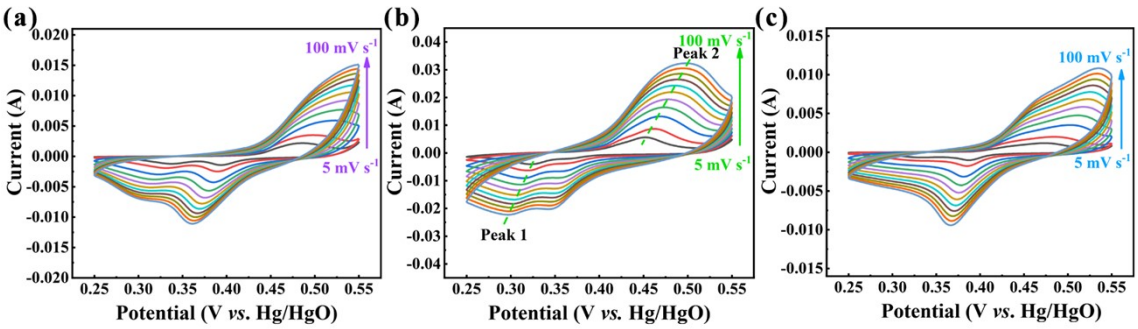

Fig. S5. CV curves of (a) $Bi_2Fe_4O_9$, (b) $Bi_2Fe_4O_9$@$Bi_{25}FeO_{40}$ and (c) $Bi_{25}FeO_{40}$ at different scan rates (5-100 mV s^{-1}).

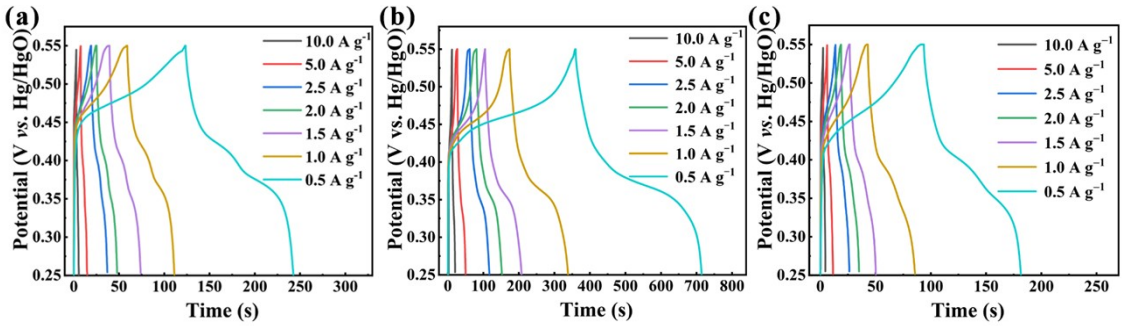

Fig. S6. GCD curves of (a) $Bi_2Fe_4O_9$, (b) $Bi_2Fe_4O_9$@$Bi_{25}FeO_{40}$ and (c) $Bi_{25}FeO_{40}$ at various current densities.

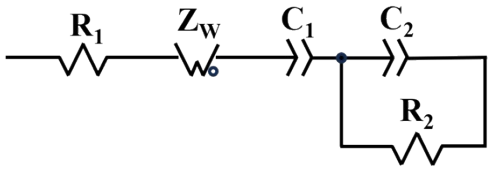

Fig. S7. Equivalent circuit diagram of EIS for the samples.

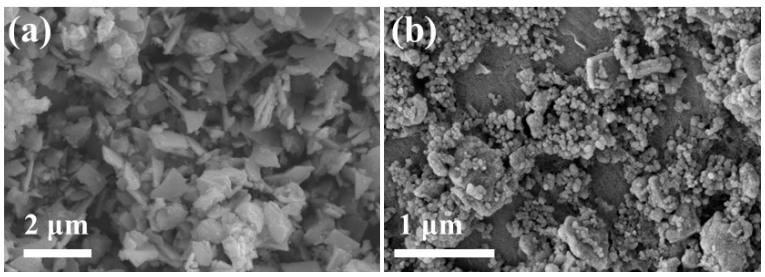

Fig. S8. SEM images of $Bi_2Fe_4O_9$@$Bi_{25}FeO_{40}$ (a) before and (b) after 3000 cycles.

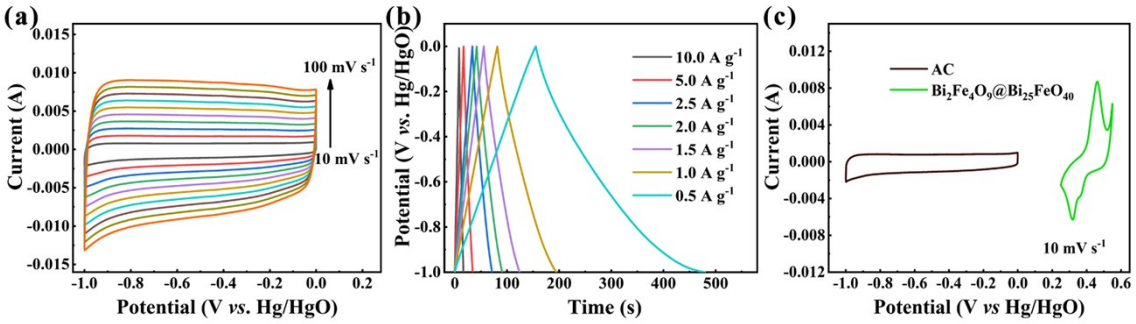

Fig. S9. (a) CV curves at scan rates of 10–100 mV s^{-1} and (b) GCD curve at current densities of 0.5–10.0 A g^{-1} for AC. (c) CV curves of $Bi_2Fe_4O_9$@$Bi_{25}FeO_{40}$ and AC at a current density of 10 mV s^{-1}.

Table S1. Fitting results of XPS high-resolution spectra for $Bi_2Fe_4O_9$@$Bi_{25}FeO_{40}$, $Bi_2Fe_4O_9$ and $Bi_{25}FeO_{40}$.

Sample	Binding energy (eV)						
	Bi $4f_{7/2}$	Bi $4f_{5/2}$	Fe $2p_{3/2}$	Fe $2p_{1/2}$	O_L	O_V	O_A
$Bi_2Fe_4O_9$	158.4	163.7	708.0 710.2	721.5 723.8	529.5	531.5	533.8
$Bi_2Fe_4O_9$@$Bi_{25}FeO_{40}$	156.3 158.4	161.6 163.7	707.6 709.9	721.0 723.5	529.3	531.4	535.1
$Bi_{25}FeO_{40}$	158.3 159.8	163.7 165.2	709.4 711.2	723.1 724.7	531.3	537.2	532.8

Table S2. Specific capacitances of $Bi_2Fe_4O_9$, $Bi_2Fe_4O_9$@$Bi_{25}FeO_{40}$ and $Bi_{25}FeO_{40}$ at different current densities.

Sample	Specific capacitance (F g^{-1}) at various current densities (A g^{-1})						
	0.5	1.0	1.5	2.0	2.5	5.0	10.0
$Bi_2Fe_4O_9$	196.6	173.3	168.7	153.8	146.5	116.6	88.5
$Bi_2Fe_4O_9$@$Bi_{25}FeO_{40}$	591.8	550.8	515.2	475.5	463.8	397.3	291.2
$Bi_{25}FeO_{40}$	145.6	142.6	119.0	109.6	104.6	88.3	70.0

Table S3. Fitting results of equivalent circuit for three samples. R_1, Z_W, C, n, R_2, and τ_0 denote the internal resistance, Warburg resistance, conductance in the constant-phase element, phase-angle exponent, charge-transfer resistance, and eigentime of the diffusion process, respectively.

Sample	R_1 (Ω)	Z_w (Ω)	C_1 (mF s^{n-1})	n_1	R_2 (Ω)	C_2 (mF s^{n-1})	n_2	τ_0
$Bi_{25}FeO_{40}$	1.78	5.89	2.23	0.87	4.83	2.69	1.01	34
$Bi_2Fe_4O_9$@$Bi_{25}FeO_{40}$	0.77	3.04	3.42	0.79	2.01	2.48	1.19	26
$Bi_2Fe_4O_9$	1.41	6.39	2.88	0.84	2.27	3.58	1.14	41

Table S4. Comparison of electrochemical performances of $Bi_2Fe_4O_9$@$Bi_{25}FeO_{40}$ and some other Bi-Fe-O based electrode materials.

Electrode material	Current density (A g^{-1})	Specific capacitance (F g^{-1})	Cycle number	Capacitance retention (%)	Ref.
$Bi_2Fe_4O_9$	1.0	443.8	5000	142.1	6
Mn-doped $Bi_2Fe_4O_9$	1.0	487	5000	87.7	7
Co doped $Bi_{25}FeO_{40}$/$BiFeO_3$	1.0	605.16	10000	87	8
$Bi_{25}FeO_{40}$ microcubes	4.0	240	5000	74	9
Zn-doped $BiFeO_3$	0.5	223	10000	85.8	10
$Bi_2Fe_4O_9$@$Bi_{25}FeO_{40}$	1.0	550.8	3000	75	This work

Table S5. Energy and power densities of the $Bi_2Fe_4O_9$@$Bi_{25}FeO_{40}$//AC ASC and some previously reported high-performance supercapacitors

Supercapacitor	Potential window (V)	Energy Densities (Wh kg^{-1})	Power densities (W kg^{-1})	Ref.
$NiMoO_4$/$CoMoO_4$ NSAs	0-1.5	27.58	636.06	11
$CuCo_2S_4$@$CoMoO_4$	0-1.4	45.73	198.8	12
N doped Fe_2N@Fe_3O_4	0-1.65	28.6	825.0	13
MoO_3-Fe_2O_3//AC	0-1.5	43.3	600	14
$Bi_2Fe_2Mn_2O_{10}$	0-1.6	48	480	15
$ZnMn_2O_4$//AC	0-1.7	54.1	794.96	16
Bi_2O_3@$NiCo_2O_4$	0-1.6	24	800	17
Fe_2O_3/r-GO/GCN	0-1.4	40	929	18
CNO-ZnO//ZnO	0-1.8	10	8100	19
ZnO@MnO_2	0-2.0	17	6500	20
Ni_3S_2/MnO_2	0-1.5	10.9	787.6	21
ZnO/CoO@NiCoS	0-1.6	39.2	399.7	22
$Bi_2Fe_4O_9$@$Bi_{25}FeO_{40}$	0-1.6	14.22	400	This work

References

1. Y. Zhang, Y. Zhao, S. Cao, Z. Yin, L. Cheng and L. Wu, *ACS Appl. Mater. Interfaces*, 2017, **9**, 29982-29991.
2. X. Wu, X. Yu, Z. Zhang, H. Liu, S. Ling, X. Liu, C. Lian and J. Xu, *Adv. Funct. Mater.*, 2023, **33**.
3. Z. Ai, L. Li, M. Huang, X. Su, Y. Gao and J. Wu, *Adv. Funct. Mater.*, 2023, **33**.
4. L. Wang, Y. Ma, M. Yang and Y. Qi, *Appl. Surf. Sci.*, 2017, **396**, 1466-1471.
5. N. Zhang, N. Gao, C. Fu, D. Liu, S. Li, L. Jiang, H. Zhou and Y. Kuang, *Electrochim. Acta*, 2017, **235**, 340-347.
6. B. Cheng, X. Li, H. Li, W. Zhang, R. Han, Y. Zhang and J. Xiang, *J. Energy Storage*, 2024, **79**, 110137.
7. H. Kuzhandaivel, Y. Selvaraj, M. C. Franklin, S. Manickam and K. Sivalingam Nallathambi, *New J. Chem.*, 2021, **45**, 15223-15233.
8. Y. Selvaraj, H. Kuzhandaivel, K. S. Nallathambi and V. Elayappan, *Energy Fuels*, 2023.
9. A. Muthu Kumar, V. Ragavendran, J. Mayandi, K. Ramachandran and K. Jayakumar, *Mat. Sci. Semicon. Proc.*, 2024, **177**, 108357.
10. S. Yu, C. Yang, W. Wang, D. Han, W. Qi, R. Ling, S. Xu and G. Liu, *J. Ind. Eng. Chem.*, 2024, **138**, 415-423.
11. C. V. V. M. Gopi, S. Sambasivam, K. V. G. Raghavendra, R. Vinodh, I. M. Obaidat and H.-J. Kim, *J. Energy Storage*, 2020, **30**, 101550.
12. X. Mao, Y. Wang, C. Xiang, D. Zhan, H. Zhang, E. Yan, F. Xu, X. Hu, J. Zhang, L. Sun and Y. Zou, *J. Alloys Compd.*, 2020, **844**, 156133.
13. J. Lee, T. S. Lim, S. G. Jo, S. Jeong, H.-j. Paik, I. W. Ock, S. Lee, K. J. Yu and J. W. Lee, *Chem. Eng. J.*, 2023, **476**, 146515.
14. S. Sundaresan, D. Subramanian and G. Raju, *Inorg. Chem. Commun.*, 2023, **148**, 110360.
15. D. Ali, F. Ashiq, I. Muneer, H. M. Fahad, A. Waheed, M. Z. Butt, R. Ahmad and M. F. M. R. Wee, *Electrochim. Acta*, 2023, **464**, 142863.
16. F. Zuo, H. Xie, J. Gao, K. Chen, H. Yang, K. Wang, L. Meng and H. Liu, *Appl. Surf. Sci.*, 2024, **669**, 160395.
17. Z. Yu, S. Wang, Y. Huang, Y. Zou, F. Xu, C. Xiang, J. Zhang, J. Xie and L. Sun, *J. Energy Storage*, 2022, **55**, 105486.
18. G. Mummoorthi, S. Arjunan, M. Selvaraj, S. L. Rokhum, N. Mani, S. Periyasamy and R. Rajendran, *Surf. Interfaces*, 2023, **41**, 103166.
19. D. Mohapatra, S. Parida, S. Badrayyana and B. K. Singh, *Appl. Mater. Today*, 2017, **7**, 212-221.
20. A. V. Radhamani, K. M. Shareef and M. S. R. Rao, *ACS Appl. Mater. Interfaces*, 2016, **8**, 30531-30542.
21. A. Thejas Prasannakumar, R. R, J. Cherusseri, R. R.Mohan and S. J. Varma, *J. Energy Storage*, 2022, **55**, 105723.
22. Y. He, X. Zhou, S. Ding, Q. Hu, D. Lin and X. Wei, *J. Alloys Compd.*, 2021, **875**, 160046.